ACS APPLIED MATERIALS & INTERFACES

www.acsami.org

Research Article

Comprehensive Study of Zr-Doped Ni-Rich Cathode Materials Upon Lithiation and Co-Precipitation Synthesis Steps

Mattia Colalongo, Basit Ali, Isaac Martens, Marta Mirolo, Ekaterina Laakso, Cesare Atzori, Giorgia Confalonieri, Peter Kus, Anna Kobets, Xiangze Kong, Tobias Schulli,* Jakub Drnec,* Timo Kankaanpää, and Tanja Kallio*

Cite This: https://doi.org/10.1021/acsami.4c05058

Read Online

ACCESS | Metrics & More | Article Recommendations | Supporting Information

ABSTRACT: Ni-rich layered oxides $LiNi_{1-x-y}Mn_xCo_yO_2$ (NMC811, $x = 0.1$ and $y = 0.1$) are considered promising cathode materials in lithium-ion batteries (LiBs) due to their high energy density. However, those suffer a severe capacity loss upon cycling at high delithiated states. The loss of performance over time can be retarded by Zr doping. Herein, a small amount of Zr is added to NMC811 material via two alternative pathways: during the formation of the transition metal (TM) hydroxide precursor at the co-precipitation step (0.1%-Zr-cp) and during the lithiation at the solid-state synthesis step (0.1%-Zr-ss). In this work, the crystallographic Zr uptake in both 0.1%-Zr-ss and 0.1%-Zr-cp is determined and quantified through synchrotron X-ray diffraction and X-ray absorption spectroscopy. We prove that the inclusion of Zr in the TM site for 0.1%-Zr-cp leads to an improvement of both specific capacity (156 vs 149 mAh/g) and capacity retention (85 vs 82%) upon 100 cycles compared to 0.1%-Zr-ss where the Zr does not diffuse into the active material and forms only an extra phase separated from the NMC811 particles.

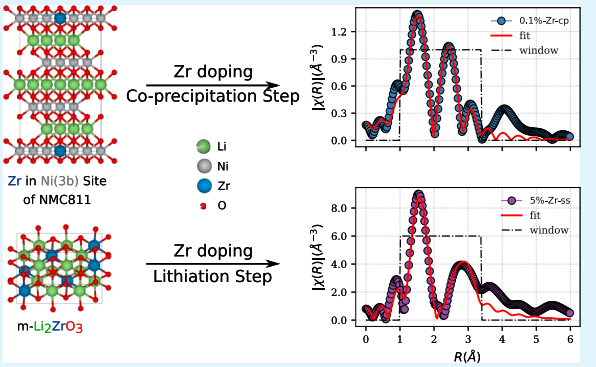

KEYWORDS: *NMC811, Zr doping, EXAFS, synchrotron radiation, HR-XRD*

1. INTRODUCTION

Lithium-ion batteries (LiBs) are regarded as the most competitive candidates for electric vehicles (EVs) because of their high energy density as compared to other zero-emission energy storage devices.[1] The necessity of long mileage by EVs pushed the industry and the scientific community to develop new cathode materials that ensure higher energy densities (Wh/L) as compared to the widely used $LiCoO_2$.

Attractive candidates with a specific capacity >200 mAh/g in a rather wide working voltage range of 3.0−4.4 V are Ni-rich cathode materials, such as $LiNi_{x-y-z}Mn_yCo_zO_2$ ($x + y + z = 1$, $x \geq 0.6$), which are considered the best candidates for next-generation LiBs.[2] Specifically, among the wide range of chemistries available, $LiNi_{0.8}Mn_{0.1}Co_{0.1}O_2$ (NMC811) shares a lower amount of Co, leading to a more environmentally friendly electrode material.

Although the premises on the advantages are proven and accepted, NMC811 still suffers from capacity loss by multiple degradation mechanisms. In fact, the intrinsic structure instability of the lattice is due to the H2 → H3 phase transition at high potentials ∼4.2 V vs Li/Li^+.[3,4] This phase transition is ascribed to a drastic change in the unit-cell volume along the *c*-axis,[5] leading to an anisotropic lattice collapse, causing cracks and electrolyte penetration in the particles.[6−8] Moreover, at high potentials, close to the material surface, Ni^{2+} is oxidized to Ni^{4+}, which reacts with the electrolyte forming an inactive rock salt phase.[9,10]

Furthermore, during synthesis and electrochemical reaction, Li^+ diffuses in the TM layers and TM migrates into the Li layer.[11] This well-known phenomenon also known as Li^+/Ni^{2+} cation mixing, negatively affects the electrochemical performances of layered materials.[12] In order to suppress Li^+/Ni^{2+} cation mixing, reduce the structural changes due to Ni^{4+} formation, and improve the structural stability of the active material, bulk doping in the host structure has been investigated by Zr^{4+} cation introduction.[13,14] Liu et al. and Schipper et al. suggested that an effective way of bulk doping is obtained when the annealing temperature through calcination is ≥700 °C. Part of the stabilization has been attributed to the formation of Zr−O bonds in the TM site (3b) that have been found to be stronger compared to Ni−O, Co−O, and Mn−O by density functional theory (DFT) calculations[13,15] and the

Received: March 27, 2024
Revised: May 5, 2024
Accepted: May 7, 2024

better structural stability when Zr^{4+} occupies the octahedral Li^+ site (3a) acting as a supporting pillar when a large amount of lithium is withdrawn during the charging process, particularly at high voltages. Although Zr doping in the TM (3b) or Li^+ (3a) site is highly desirable, Zr^{4+} does not have any preferred optimized geometry according to both crystal field stabilization energy and octahedral site stabilization energy because of its d^0 electronic configuration.[16] Therefore, the Zr-dopant location after synthesis remains still a debatable subject, yet it is not fully understood. Previous efforts have been made to locate the dopant in the structure,[13,17,18] however, although the exact position of Zr in the unit cell has been proposed based on DFT calculations, it has not yet been experimentally proven.

In this study, we clarify the role of Zr doping after the synthesis through two different pathways. The bulk doping is investigated first during the lithiation step, where Li is added during the calcination process through the presence of lithium source (LiOH) and the precursor $Ni_{0.8}Mn_{0.1}Co_{0.1}(OH)_2$ ($NMC(OH)_2$) and, second, by doping the precursor $Ni_{0.8}Mn_{0.1}Co_{0.1}Zr_{0.001}(OH)_2$ ($NMCZr(OH)_2$) during the co-precipitation step.[19]

In the latter way, the dopant is added as a salt with the other precursors' transition metals (TMs) during the first stage of the synthesis. By means of structural studies using synchrotron radiation, we are able to identify that through the lithiation step Zr^{4+} does not diffuse in the active material and forms an inactive m-Li_2ZrO_3 extra phase, even when the dopant is added in traces. However, by following the co-precipitation route, Zr^{4+} is found in the octahedral site of NMC811, which improves the electrochemical stability upon cycling. The decision to employ trace amounts of the dopant is based on the electrochemical inactivity of Zr^{4+} and the consequent reduction in the amount of the electroactive elements in the host material in the case of substitutional doping. This would inevitably lead to a decrease of discharge capacity when the Zr^{4+} concentration is excessively high.[20] Furthermore, compared to other studies on Zr bulk doping, we are able to identify with spectroscopy measurements the position of the dopant in the unit cell of NMC811. We believe that the study described herein widens the understanding of Zr doping in high energy density cathode materials, allowing researchers to follow up on a preferred path in order to effectively dope the material and improve its stability.

2. EXPERIMENTAL SECTION

2.1. Material Synthesis. The precursor material $NMC(OH)_2$ and the Zr-doped $NMCZr(OH)_2$ have been synthesized via the co-precipitation method by Umicore Battery Materials Finland. $Ni_{0.8}Mn_{0.1}Co_{0.1}(OH)_2$ is then mixed with LiOH (Thermo Fisher, Anhydrous, 98%) in a 1:1.005 ratio in a mortar and gently ground together with a pestle for 20 min to obtain a homogeneous distribution between the powders. The mixture is calcinated at 800 °C under an O_2 atmosphere with a flow of about 100 mL/min^{-1} for 12 h in order to obtain $LiNi_{0.8}Mn_{0.1}Co_{0.1}O_2$ (hereinafter undoped) used as a reference material. To synthesize 0.1%-Zr-ss and 5%-Zr-ss, the precursor, LiOH and $Zr(OH)_4$ (Sigma-Aldrich, 97%) as a dopant source have been mixed together in 1:1.005:0.001 and 1:1.005:0.05 molar ratio and ground with a pestle for 20 min and calcinated at 800 °C under O_2 flow for 12 h. Finally, the doped precursor is lithiated through calcination (0.1%-Zr-cp) at 800 °C under O_2 flow for 12 h by adding LiOH in a molar ratio of 1.005 compared to the precursor. A slight excess of lithium is meant to overcome Li loss during the long calcination process. A schematic representation of the synthesis is reported in Figure S1 and all the used compounds weights have been reported in Table S1.

2.2. Electrodes Preparation and Testing. NMC811 electrode preparation uses 93 wt % of an active material (undoped, 0.1%-Zr-ss, or 0.1%-Zr-cp), 3 wt % conductive carbon (Timcal Super C65), and 4 wt % polyvinylidene fluoride (Solvay, Solef 5130) in *N*-methyl-2-pyrrolidone (NMP from BASF, Life Science). The slurry was cast on an Al foil (MTI Corporation, 18 μm thickness) with a doctor blade and an electrode thickness of ~120 μm. The paste was dried overnight in the fume hood and then heated for 4 h at 80 °C into an oven to remove the last NMP residuals. Electrodes were cut into 14 mm diameter discs and calendered with a pressure of 3248 kg/cm^2 for 10 s to ensure better mechanical stability and electronic conductivity.

The 14 mm cut electrodes have been dried for 8 h at 80 °C before being transferred in an Ar-filled glovebox (Jacomex, O_2 and H_2O level <1 ppm) avoiding air exposure during the process. Half-cells (CR-2016 type, Hohsen casing) were assembled, where the working electrodes were undoped with 0.1%-Zr-ss and 0.1%-Zr-cp electrodes, whereas the counter electrode was a 16 mm cut of Li^0 (Alfa Aesar, 0.75 mm thick). The sandwich was separated by 18 mm glass fiber discs (GF/A, Whatmann) and soaked in 200 μL of $LiPF_6$ (1 M) in 1:1 ethylene carbonate:dimethyl carbonate (EC:DMC, from BASF), known as LP30 electrolyte. The rate capability tests were performed using the constant current charge and discharge method in the voltage range of 3.0 to 4.4 V. The calculated applied current for charging cycles above 0.2 C rates was equal to 0.2 C. For rate capability tests, it is fundamental to slowly charge each cell, thus upon discharge they will all start from the same state of charge. Therefore, cells cycled at 0.5, 1, 2, and 5 C are charged with 0.2 C current and discharged at 0.5, 1, 2, and 5 C, respectively. Long-term cycling half-cells are charged and discharged at the same current rate. More details regarding the cycling strategy for the two modes are disclosed in Supporting Information Figure S26. All of the measurements were carried out using the cycling station Landt Cycler (model CT3002 AU). The *C*-rate current applied was calculated considering the electrode weights and 70% of the NMC811 theoretical capacity, which was 190 mAh/g. For full-cell long-term cycling tests, a 14 mm positive electrode was balanced with an 18 mm diameter graphite electrode (a single-side coated commercial graphite sheet with a coating thickness of 41 μm and a composition of 93.2% graphite, 2.5% conductive carbon "Super P" and binder 2.5% SBR and 1.8% CMC; MTI corp, USA). A 19 mm polyolefin separator (Celgard) and 13 wt % $LiPF_6$ in 20:25:40 wt % EC/DMC/EMC (ethyl methyl carbonate) with a 2 wt % vinylene carbonate electrolyte (ELYTE, Germany) were used for the measurements. Capacity balancing of the anode and cathode (N/P ratio) was set to ~1.3−1.4:1. The assembled full cells were studied by galvanostatic charge−discharge tests with a Landt battery cycler (Wuhan Land, China) at 1 C in the potential range of 2.9−4.3 V vs graphite at room temperature. Five formation cycles at 0.1 C between 2.9 and 4.2 V vs graphite were done and are reported in Figure S28.

2.3. X-ray Diffraction Data Collection. High-energy powder diffraction (HE-XRD) data were collected at the ID31 beamline at the European synchrotron radiation facility (ESRF), where a 2D CdTe 2 M Pilatus detector was used in a Debye−Sherrer geometry. The unfocused beam size was ~100 μm and the incident beam energy was 75 keV. Although 2D detectors are fast in collecting a full pattern, reducing exposure time and radiation damage, the resolution of ID31 is limited by the beam bandwidth ($\frac{\Delta E}{E} = 0.3\%$). Therefore, to appreciate even the smallest variations in the samples high-resolution powder diffraction data (HR-XRD) at the ID22 beamline at ESRF (European synchrotron radiation facility)[21] were collected. It was equipped with a Si(111) multianalyzer in Bragg−Brentano geometry. The beam energy was set to 35 keV. The undoped, 0.1%-Zr-ss, 0.1%-Zr-cp, and 5%-Zr-ss powders were packed in spinning Kapton capillaries of 0.5 mm in diameter and the diffraction patterns were collected using a 5× larger beam of 1 mm^2 compared to ID31 setup. Measurements were performed using an Eiger2 X CdTe 2M-W detector preceded by 13 Si(111) analyzer crystals, collecting and averaging four different spots of the capillary. Furthermore, Si powder

https://doi.org/10.1021/acsami.4c05058
ACS Appl. Mater. Interfaces XXXX, XXX, XXX−XXX

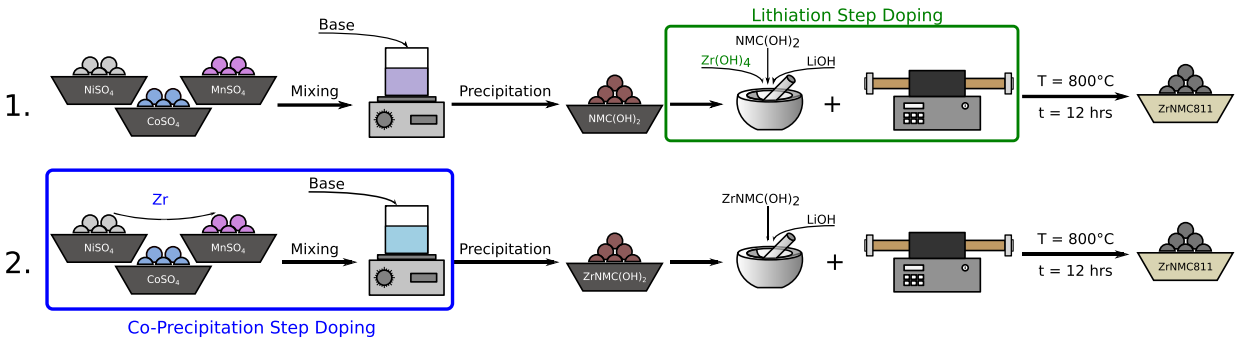

Figure 1. Representative sketch of the Zr-doping process through two synthesis steps: either upon lithiation step using $Zr(OH)_4$ (1), or upon co-precipitation step (Zr) (2).

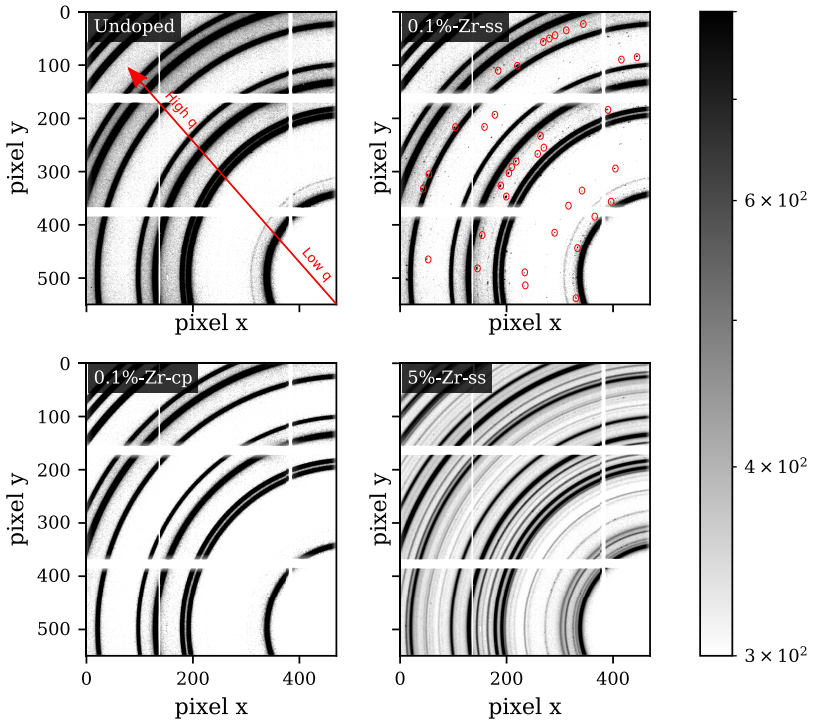

Figure 2. Detector Image portion of the XRD patterns of undoped, 0.1%-Zr-ss, 0.1%-Zr-cp, and 5%-Zr-ss. In 0.1%-Zr-ss, circles in red show the detection of an extra-phase speckle. For 5%-Zr-ss, darker rings refer to the NMC811 phase, and gray rings also refer to the appearance of an extra phase. Because of 5% dopant addition, the intensity and the concentration of the extra phase are higher, explaining the transition from speckle to ring texture as the crystallographic population increases.

has been used as a reference sample for fitting the instrumental broadening in GSAS-II Software.[22]

2.4. X-ray Spectroscopy Data Collection. Experimental Zr K-edge X-ray absorption spectroscopy (XAS) data were measured at the BM23 beamline at ESRF.[23] Because of the high dilution of Zr in all the doped samples, the spectra were collected in fluorescence mode. The powders were pressed into 13 mm pellets with a 20 mm die hydraulic press machine (SPECAC) and mounted on an Al holder. Multiple spectra per sample were collected and averaged/summed to increase the signal-to-noise ratio, especially in the EXAFS mode, in the energy range of the Zr K-edge +500 eV. A Zr foil after the sample was used as a reference to calibrate the data collected from the beamline. Pellets preparation details are shown in Table S8. The X-ray absorption near-edge structure (XANES) data processing was performed using Athena software, while the fit of the data was performed using the Artemis plugin called FEFF. Both softwares are included in the Demeter package developed by Ravel et al.[24] The normalized spectra were FT plotted in a k-range of 2−10 $Å^{-1}$. The path-fitting contribution for zirconium−oxygen (Zr−O), zirconium−metal (Zr−M), and zirconium−Zirconium (Zr−Zr) bonds is extracted from the cif structures of $LiNiO_2$ and m-Li_2ZrO_3. For the former cif, the scattering Zr paths are generated by manually substituting Zr to Ni in the TM site (3b) and Zr to the Li site (3a). However, since fractional amounts are not accepted by IFFEFIT path extraction, the manual substitution is done in a 2 × 2 × 2 supercell with removed symmetry, the used crystal structures can be visualized in Supporting Figure S18. The value of the amplitude reduction factor (S_0^2) for Zr was obtained from the fitting of the corresponding Zr metal foil used as a reference and fixed in the fit process of the cathode materials. More details regarding the Zr metal foil fit are reported in Supporting Information, Figure S28.

2.5. TEM, XRF, and ICP Measurements. To prepare the TEM samples for undoped, 0.1%-Zr-ss, and 0.1%-Zr-cp, a focused ion beam (FIB, JIB-4700F, JEOL) was used to cut the cathode material into thin slices approximately 50 nm thick. For a fair comparison, homogeneous particles were chosen in size for all the samples, i.e., undoped, 0.1%-Zr-ss, and 0.1%-Zr-cp to achieve a thin lamella. Afterward, the chosen particles (undoped, 0.1%-Zr-ss, and 0.1%-Zr-cp) were covered by a protective layer of platinum (Pt) in order to protect it during the fine milling from high voltage focused ion beam.

https://doi.org/10.1021/acsami.4c05058
ACS Appl. Mater. Interfaces XXXX, XXX, XXX−XXX

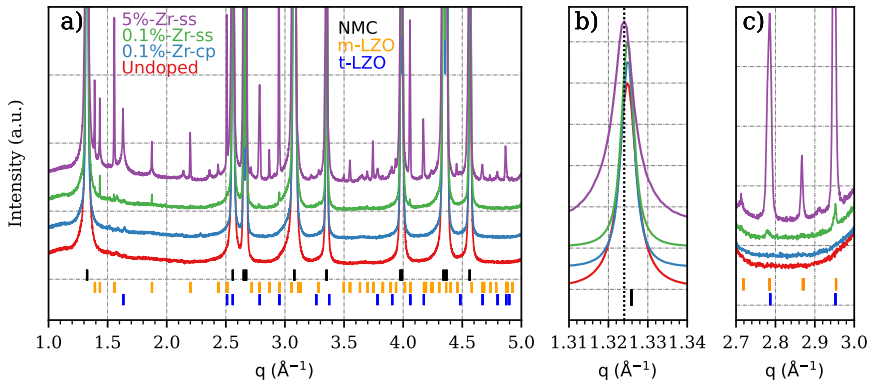

Figure 3. (a) High-resolution XRD of NMC811 with different Zr dopings averaged on four spots of the Kapton capillary. (b) Magnified region of NMC811 003 peak shift. (c) Enlarged area for displaying the formed extra phases. (a, b, c) Black ticks index NMC peaks, orange ticks refer to *m*-Li_2ZrO_3 (m-LZO) peak positions, and blue ticks are assigned to the *t*-Li_2ZrO_3 (t-LZO) phase.

Zr and Li sample proportions were determined through inductively coupled plasma-optical emission spectroscopy (ICP-OES), using a Thermo Scientific iCAP 6000 Series instrument. whereas major metals, manganese, nickel, and cobalt, were analyzed using K2S2O7 fusion and X-ray fluorescence (XRF) method with PANanalytical Axios Max instrument

3. RESULTS AND DISCUSSION

3.1. X-ray Diffraction. For studying the Zr doping effect on NMC811, one co-precipitation doping sample containing 0.1 mol % of Zr was synthesized, hereinafter 0.1%-Zr-cp. In addition, two samples were doped during the lithiation step, one with 0.1 mol % of Zr (hereinafter 0.1%-Zr-ss) and a second one with 50 times more Zr (hereinafter 5%-Zr-ss). The 5%-Zr-ss is supportive of understanding the Zr phase composition formed during the lithiation. A schematic representation of the synthesis resulting in secondary particles with a mean diameter of ∼8−10 μm is found in Figure 1. It is important to stress here that the morphology of both $ZrNMC(OH)_2$ precursors was carefully controlled to yield similar structures as this is well-known to have major effect on the electrochemical behavior. As a reference, an undoped sample is also present; for more details on the synthesis process refer to the Section 2.1. To verify the exact chemical composition and the Li, Zr, Ni, Mn, and Co ratios among the samples, ICP-OES and XRF measurements were performed. As reported in Table S9, the samples share the same Ni, Mn, and Co metal ratios, Li atomic ratio is close to 1 for all, while 0.1%-Zr-ss and 0.1%-Zr-cp reasonably share similar Zr amount.

Based on X-ray diffraction (XRD) measurements with a 2D detector as displayed in Figure 2, the undoped NMC811 is present as a pure phase, as the visible diffraction rings can be assigned to the NMC811 phase only. However, by the addition of $Zr(OH)_4$ during the lithiation step, a new phase appears that is visible as diffraction speckles and is circled in red in Figure 2 (0.1%-Zr-ss). Considering the size of the beam, the speckles suggest that new phase crystals have a size ≥100 μm. In the case of higher doping concentration, 5%-Zr-ss in Figure 2, more intense and uniform rings emerge, indicating multiple extra phases and a higher concentration of it. Regarding the 0.1%-Zr-cp sample, no extra phases are found; in fact, as shown in Figure 2, the powder pattern is as clean as for the undoped sample.

To further improve the quality of the data and detect possible not-found extra phases for 0.1%-Zr-cp, high-resolution XRD (HR-XRD) was used. Compared to HE-XRD, this time, the Kapton capillaries were spun to avoid preferential orientation, the size of the beam was increased from 100 μm to 1 mm to improve the measured statistics, and additionally, four different spots were sampled to investigate possible heterogeneities in the sample. The HR-XRD results are listed in Figure 3a. The peaks assigned to ticks in black are related to the known *R*3-*m* layered structure space group, which belongs to NMC811, whereas yellow ticks, define the crystallographic reflections of *m*-Li_2ZrO_3, which is an extra phase found previously in other Zr-based studies.[25,26] It is interesting to notice that in exact contrast to what Gao et al.[27] found by Zr doping through a sol−gel method, in the solid-state synthesis, *m*-Li_2ZrO_3 is present even at low concentrations as seen for the 0.1%-Zr-ss sample. As doping concentration increases (as per 5%-Zr-ss) a new Zr-based polymorph appears. As shown in Figure 3a, the blue ticks are assigned to the metastable phase *t*-Li_2ZrO_3. Although the latter polymorph was characterized by Quintana et al.[28] at temperatures above 1100 °C, this metastable symmetry can also exist at temperatures below 800 °C.[29,30] The former extra phase belongs to the *C*/2*m* space group (a = 5.42401 Å, b = 9.02166 Å, c = 5.42021 Å and β = 112.59°) and the latter to the *I*4/*amd* space group (a = 4.25582 Å, c = 9.01793 Å).[28] However, we were not able to index the phase of the two peaks present for the 5%-Zr-ss sample at 2.142 and 2.363 $Å^{-1}$. In Figure 3b, undoped, 0.1%-Zr-ss, and 0.1%-Zr-cp do not show any significant peak shift variation. However, for high doping concentration, the 003 peak related to the *c*-axis parameter of the NMC811 unit cell slightly shifts to lower *q*-values. A shift to lower *q*'s is, often, related to the inclusion of the dopant in the unit cell[25] as a consequence of the unit-cell expansion. However, also a consistent lack of Li^+ in NMC811 withdrawn by *m*-Li_2ZrO_3 and *t*-Li_2ZrO_3, for 5%-Zr-ss, might generate a cell expansion. The latter phenomenon is due to the lack of Li in the Li sites, which eases the TM migration in the Li layers. Therefore, a higher Ni^{2+}/Li^+ cation mixing leads also to a volume increase of the unit cell.[31]

To quantify the share of the $Zr(OH)_4$ precursor forming the zirconium containing extra phase(s) during the lithiation step in the 0.1%-Zr-ss sample, a direct comparison method for multiphase determination and Rietveld refinement are used. Details on the peak integration calculation and refinement are disclosed in Supporting Section 2.1. In fact, during the lithiation step, for 0.1%-Zr-ss, even though a trace of Zr is added as $Zr(OH)_4$, 100% of $Zr(OH)_4$ transforms into *m*-

https://doi.org/10.1021/acsami.4c05058
ACS Appl. Mater. Interfaces XXXX, XXX, XXX−XXX

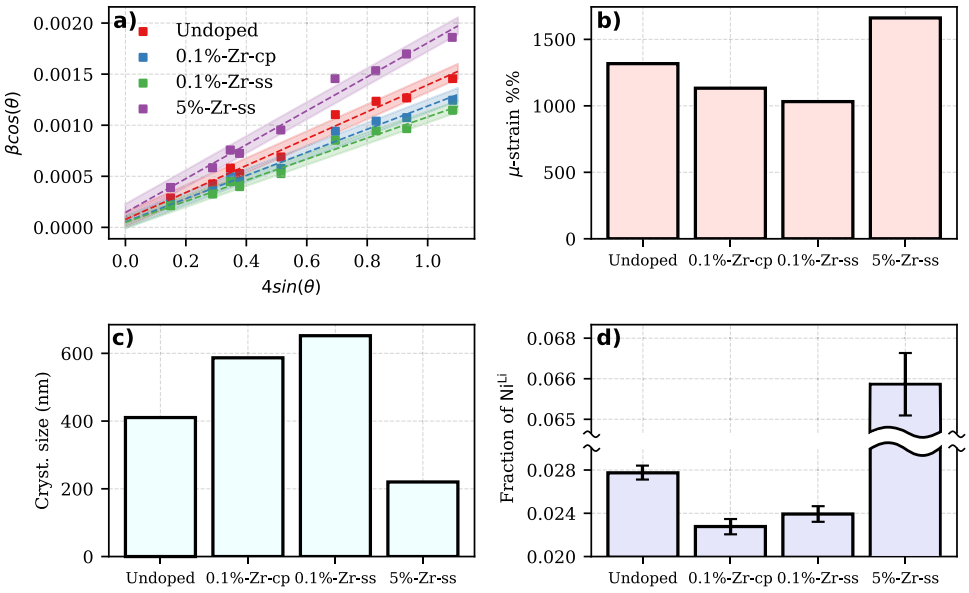

Figure 4. (a) W−H plot based on nine NMC reflections. All the R^2 from the linear regression are >0.9. Filled parts represent the σ of the fit. (b) μ_{strain} calculated from the slope of the linear fitting, (c) crystal size from the y-intercept, and (d) cation mixing (here expressed as fraction of Ni(3b) in Li(3a) sites) calculated from Rietveld refinement.

Li_2ZrO_3 within an absolute estimated error of 0.01 mol %. The high precision character of the quantitative characterization carried out for the XRD data was endorsed by a fourth-generation synchrotron photon source and the use of an analyzer crystal, which reduced the scattering from air and suppressed the background from sample fluorescence. Therefore, this clearly indicates that Zr is not prone to diffuse into the active material phase, but rather finds a more thermodynamically stable structure outside the NMC811 particles. This could be attributed to Zr^{4+} large ionic radius and high valence, preventing the specimen to migrate in the bulk phase at the given temperature.[32] Moreover, in this work, the amount of the extra phase can be estimated reliably by peak integration only for the sample 0.1%-Zr-ss.

Unfortunately, for 5%-Zr-ss the phase estimation is rather cumbersome since the diffraction intensity of both $11\bar{1}$ and 002 reflections of the m-Li_2ZrO_3 phase increases more than expected. We assume that for those specific peaks, a third phase is contributing to the overall peak intensity. It is indeed possible that at those high Zr concentrations, a third stable phase (h-Li_8ZrO_6 $R3$-m, a = 5.469 Å, and c = 15.353 Å) is formed during the synthesis.[29] The h-Li_8ZrO_6 reflections would overlap with those of m-Li_2ZrO_3, hindering a clear identification of each phase. Further efforts to analyze the relative amount of the extra phases have not been carried out as 5%-Zr-ss has no real electrochemical interest, but it is only utilized to support the phase identification for the solid-state doped sample.

Crystal size and microstrain are calculated through the Williamson Hall (W−H) plot[33] shown in Figure 4a by fitting the full width half-maxima (fwhm) of 9 NMC811 reflections at different 2θ values. Figure 4b, depicts how, compared to the undoped sample, both 0.1%-Zr-ss and 0.1%-Zr-cp have reduced internal strain. Figure 4c shows an increase in the crystal size for both 0.1%-Zr-cp and 0.1%-Zr-ss samples. Cation mixing is often calculated by the I_{003}/I_{104} ratio. However, unless proper intensity corrections are carried out, this ratio is not a reliable source.[34] In this work, to estimate the Ni^{2+}/Li^+ ratio, we refined the fractional occupancy of Ni(3b) in the Li(3a) sites applying a few constraints. In fact, the fraction variation of Li^+ and Ni^{2+} in the TM (3b) site and Li (3a) site of the $R3$-m space group is constrained as follows: $Ni^{2+}_{3b} + Ni^{2+}_{3a} = 0.8$, $Li^{+}_{3a} + Li^{+}_{3b} = 1$ and $Li^{+}_{3a} - Ni^{2+}_{3b} = 0.2$ (more details about the cation mixing evaluation is reported in Supporting Section 2.2). From Figure 4d, it can be seen how the fraction of Ni in the Li sites (Ni^{Li}) also decreases for both 0.1% doped samples. It is interesting to notice how 5%-Zr-ss has a notably smaller crystal size, increased strain, and a substantial increase in cation mixing. This defines a more disordered structure attributed to the LZO impurity formation and a substantial Li^+ percentage missing in the active material. The large amount of Ni^{2+} in Li^+ sites would justify a shift of the NMC811 reflections to lower q values.[31] However, for 0.1%-Zr-ss a drop in microstrain, cation mixing, and an increase in crystal size might suggest a Zr inclusion in the crystal structure but no peak shift in XRD in Figure 3b is observed. Moreover, it is not in agreement with the evidence that almost all Zr forms m-Li_2ZrO_3. However, one hypothesis is that Zr still forms a thin coating layer on the surface of the NMC811 particles during the lithiation step, which might affect the above-mentioned parameters and the morphology of the primary particles.[14] A second hypothesis connected to the decrease in crystallite size and strain for the 0.1%-Zr-ss sample is ascribed to the formation of m-Li_2ZrO_3. Zhu et al. demonstrated that a consistent crystalline growth of polycrystalline materials upon lithiation happens within the range from 750 to 900 °C.[35] At these temperatures, the crystal growth is mainly influenced by the evaporation of Li as Li_2O,[36] which modifies the Li/O migration in the NMC host structure. In our specific case, at 800 °C, m-Li_2ZrO_3 another lithium-based oxide is formed. A new variable that affects the Li/O migration is added to the equation. However, for small amount of Zr doping, we believe that the excess of Li^+ supplied to overcome the lithium loss, surpasses the amount of m-Li_2ZrO_3 formed, guaranteeing the amount of Li^+ in the NMC crystal structure, whereas, for 5%-Zr-ss, the excess of LiOH used during the synthesis is not

https://doi.org/10.1021/acsami.4c05058
ACS Appl. Mater. Interfaces XXXX, XXX, XXX−XXX

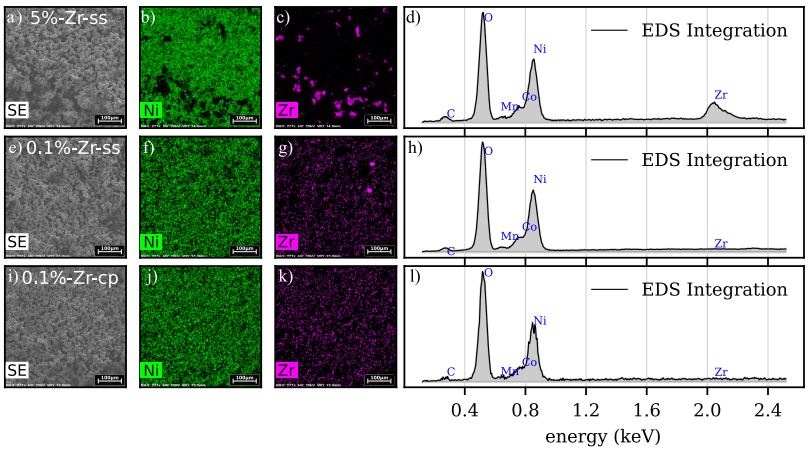

Figure 5. (a, e, i) SEM-EDX images of 5%-Zr-ss, 0.1%-Zr-ss, and 0.1%-Zr-cp, respectively, with a field of view of 500 μm, energy (HV) of 20 kV, and a working distance (WD) of 14.9 mm. In green, the elemental map of the samples for the Ni edge (b, f, j) and in pink the elemental map of the Zr edge (c, g, k). (d–l) EDS integration of the respective probed areas.

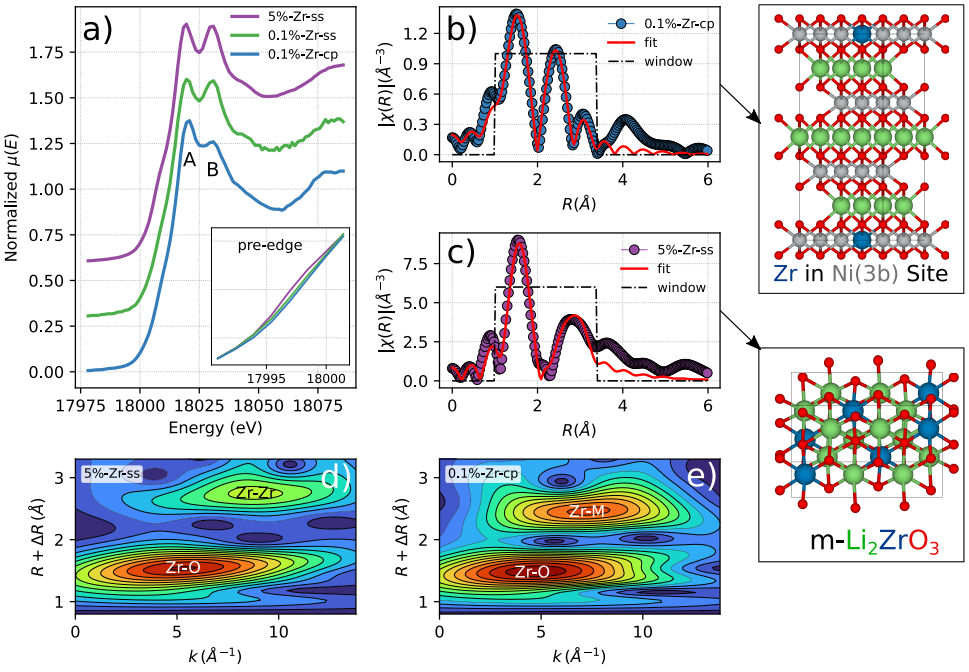

Figure 6. (a) XANES for the 0.1%-Zr-cp, 0.1%-Zr-ss, and 5%-Zr-ss samples. (b) EXAFS-FT 0.1%-Zr-cp and (c) EXAFS-FT for 5%-Zr-ss. (d, e) Wavelet-transforms of 5%-Zr-ss and 0.1%-Zr-cp, respectively.

sufficient to compensate for the *m*-Li_2ZrO_3 and *t*-Li_2ZrO_3 phases formation. A lack of Li within the host structure promotes Ni migration in the Li sites leading to a more disordered/defected structure and, consequently, smaller crystals. In fact, Ni(3b) migration in the Li(3a) sites shows a small variation for 0.1%-Zr-ss compared to the undoped sample and a drastic variation for 5%-Zr-ss as reported in Figure 4d. Confirmation of the second hypothesis for lithium migration effects still remains open, requiring further investigation. Additionally, still, no clear evidence on the location of Zr in the case of 0.1%-Zr-cp exists, i.e., when the Zr integration takes place during the co-precipitation step because there is neither a trace of extra reflections even by means of HR-XRD as depicted in Figure 3c nor peak shifts.

3.2. SEM-EDX. Scanning electron microscopy-energy dispersive spectroscopy (SEM-EDX) measurements are conducted to investigate the possible Zr distribution in the samples, although 0.1 mol % of Zr sets already a limit case scenario for EDX detection. To understand what happens to Zr during the lithiation process, the highest concentration sample (5%-Zr-ss) is first studied. In Figure 5a, a 500 μm field of view of particles ensemble is shown. Upon calcination, as clearly reported in Figure 5c, $Zr(OH)_4$ does cluster into crystal chunks that are known to be a mixture of *m*-Li_2ZrO_3 and *t*-Li_2ZrO_3 from the diffraction data in Figure 3. For more detailed information, a zoomed-in version of a typical crystal shape and size can be found in Figure S7e, where the LZO particle stands completely outside the NMC811 particles. EDX analysis of the 5%-Zr-ss particle surface was conducted and reported in Figure S7a–d in the Supporting Information), but no elemental Zr was detected. For 0.1%-Zr-ss, instead, only two isolated crystals of LZO can be detected, which do not belong to camera artifacts. Therefore, by SEM-EDX, Zr is found outside the NMC811 particles as separated crystals that

https://doi.org/10.1021/acsami.4c05058
ACS Appl. Mater. Interfaces XXXX, XXX, XXX–XXX

Table 1. FT Fitted Parameters of the EXAFS Data[a]

sample	bond	CN	R [Å]	σ^2	ΔE^0 [eV]	$S0^2$
0.1%-Zr-cp	Zr−O	6	2.117 ± 0.009	0.0038 ± 0.0015	−3.49 ± 0.94	0.86
	Zr−M	6	2.99 ± 0.01	0.0078 ± 0.0012	−3.49 ± 0.94	0.86
5%-Zr-ss	Zr−O	6	2.121 ± 0.013	0.00126 ± 0.0009	−2.78 ± 1.78	0.86
	Zr−Zr	2	3.234 ± 0.0018	0.00083 ± 0.0018	−2.78 ± 1.78	0.86

[a]Amplitude values for 0.1%-Zr-cp and 5%-Zr-ss ($S0^2$) are kept constant, and these values are extracted by the fitting of the standard Zr foil.

through XRD data are indexed as m-Li_2ZrO_3 extra phase and found to be ∼100% of the initial $Zr(OH)_4$ amount. Furthermore, for the 0.1%-Zr-cp sample, the EDX experiment does not show clustered Zr-based impurities as displayed in Figure 5k. To improve the quality of data ascribed to the Zr quantification by means of electron beam-based characterizations, TEM-EDX on sample lamellas was performed. Figure S10 displays EDX maps on two different spots of the material lamella, spot A close to the surface and spot B bulk. We could hardly identify any Zr signal for the modified samples. This is to be expected as Zr is challenging to detect with EDX-based techniques when its concentration is lower than 0.5 wt %. The absence of possible coatings for 0.1%-Zr-ss is reported in Figure S11 where a magnified region close to the surface of the 0.1%-Zr-ss sample is investigated.

3.3. X-ray Absorption Spectroscopy. To better clarify the role of Zr doping during the co-precipitation, which is unclear in both HE/HR-XRD and EDX elemental mapping, the doped samples were probed by means of XAS. XAS provides insights into the short-range order around the dopant element as a complementary technique to XRD. The XANES portion of the XAS spectra is characterized by a main peak (or white line) split into two components, A and B, as shown in Figure 6a. The doped samples possess a Zr oxidation state equal to 4^+ as shown in Supporting Figure S20, since the E_0 value in the XANES first derivative is similar to ZrO_2.

The doublet features (A and B) present in the XANES spectra shown in Figure 6a arise due to the Zr^{4+} allowed transition $1s \rightarrow 5p$. The A and B splitting is assigned to a Zr in an octahedrally coordinated site.[37,38] It is interesting to notice that for 0.1%-Zr-cp, compared to both 0.1%-Zr-ss and 5%-Zr-ss, the peak ratio of the relative intensities between features A and B increases. This observation indicates that upon the co-precipitation step the local Zr environment is different compared to the lithiation step.[39] This clear difference defines, therefore, at least two different Zr local environments for the NMC811 doped samples, both in sixfold coordination.

Furthermore, the 5%-Zr-ss sample shows a stronger pre-edge feature compared with both 0.1%-Zr-ss and 0.1%-Zr-cp samples. The pre-edge feature might arise from the presence of t-Li_2ZrO_3 as noticed by Gosh et al.,[40] which is present only in 5%-Zr-ss. However, the pre-edge feature in 5%-Zr-ss might be also ascribed to the presence of an amorphous phase[41] considering that $Zr(OH)_4$ is used upon lithiation.

To assist the interpretation of the Zr environment seen by the XANES portion of the spectrum, Fourier transform-extended X-ray absorption fine structure (FT-EXAFS) results are reported in Figure 6b,c. However, for the lithiation step, only 5%-Zr-ss is considered during the fitting process among the lithiation doped samples, since they show, by XANES, the same local environment. Furthermore, 0.1%-Zr-ss turned out not to have enough resolution at k = 10 $Å^{-1}$, as shown in Supporting Figure S17, to be considered a reliable source of data. However, for completeness of the data set, the FT-EXAFS of 0.1%-Zr-ss is reported in Supporting Information Figure S21. Considering the same amount of scans for the doped samples, the reason 0.1%-Zr-ss has less resolution in K than 0.1%-Zr-cp might be ascribed to the Zr heterogeneity in the sample. It is the case for 0.1%-Zr-ss, where the HR-XRD patterns of four different capillary spots show different intensities for the m-Li_2ZrO_3 extra-phase reflections, as displayed in Figure S6. As energy scans proceed, slight movements of the beam might be observed,[42] which causes problems in the amount of matter probed for heterogeneous samples. Based on the ICP-OES and XRF measurements for Zr quantification reported in Table S9, nonetheless, 0.1%-Zr-ss contains slightly more dopant, which is nonhomogeneously distributed.

Fortunately, 5%-Zr-ss with a higher Zr content can still be used as an interpreter for the Zr local environment and be representative of the lithiation doping step.

Consistently to the XANES assumptions, the EXAFS range shows two distinct features in the Fourier transforms assuming k_{max} = 10 Å; therefore, different atom coordination and environments for 0.1%-Zr-cp and 5%-Zr-ss are found. They both show a peak at around 1.2−2.0 Å ascribed to the Zr−O bond in the first coordination sphere. However, the two samples start to differ in the second coordination sphere between 2.0 and 3.5 Å. In fact, 0.1%-Zr-cp shows a more intense peak at ∼2.43 Å whereas 5%-Zr-ss at ∼2.81 Å, assigned to metal−metal interactions. The scattering paths for the FT fitting have been extracted from different structures such as m-Li_2ZrO_3, identified by XRD, and $LiNiO_2$, which is the closest simple structural file reminiscent to the NMC811 without fractional atomic occupancies. For the latter, the Zr is placed in plausible sites, both substitutional and interstitial, as shown in Supporting Figure S18. The fitting process for Zr in 0.1%-Zr-cp converges with the scattering paths extracted by substituting Zr in both the Ni(3b) and Li(3a) octahedral sites. However, no compatibility for the scattering paths is found for Zr in the tetragonal(6c) sites, as widely described in Supporting Information Section 4. R_{Zr-O} and R_{Zr-Ni} bond length values are compatible with the Ni−Co−Mn values in NMC811,[43] as shown in Table 1, with the interesting difference that R_{Zr-O} and R_{Zr-Ni} are larger compared to R_{M-O} and R_{M-M} (M = Ni, Co, Mn) lengths found by Erickson et al.[43] If the ionic radius of Zr^{4+} = 72 pm, Li^+ = 76 pm, and Ni^{2+} = 69 pm is merely considered in the octahedral geometry,[44] a local environment enlargement is expected when Zr is substitutional to Ni and, in contrary, a local compression if Zr is substitutional to Li(3a). As shown in Supporting Figures S14 and S15, only when Zr is in the Ni site(3b), R_{Zr-O} and R_{Zr-Ni} undergo a similar positive increase of 0.147 and 0.121 Å, respectively, to the initial guess. Although a simplistic approach, it might suggest that Zr lies down in the TM sites, since no local compression is observed.

In summary, the EXAFS data of 0.1%-Zr-cp unveil the Zr environment to be octahedrally coordinated and bond lengths compatible with the NMC811 structure. Larger R_{Zr-O} and

https://doi.org/10.1021/acsami.4c05058
ACS Appl. Mater. Interfaces XXXX, XXX, XXX−XXX

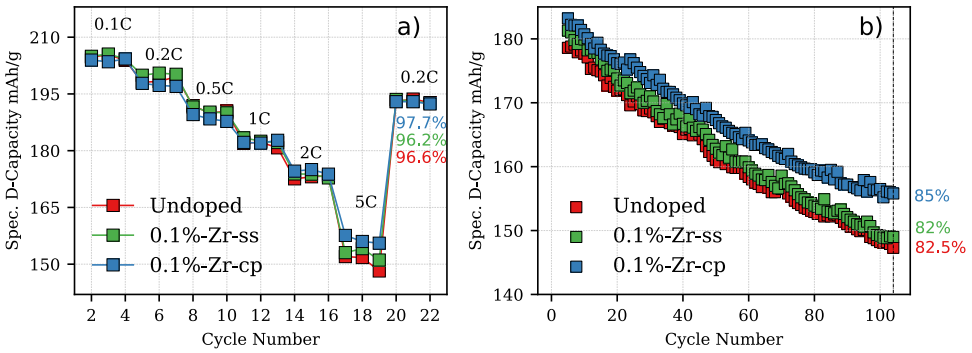

Figure 7. Electrochemistry half-cell measurements with active material loading of 2 mAh cm^{-2}. (a) Rate capability test (3.0−4.4 V voltage window) from 0.1 to 5 C and last recovery cycling at 0.2 C. (b) Long-term cycling, same voltage window at 1 C, all the cells were cycled once at 0.03 C and three times at 0.1 C (both cycles omitted) for cathode-electrolyte interface (CEI) formation.

R_{Zr-Ni}, as compared to Ni, Mn, and Co values, are in agreement with a unit-cell enlargement seen in previous studies,[45] which strengthens the Zr−O bond and increases structural stability. However, for doping traces (0.1 mol %), *macro-strain* effects might be too small to cause a clear peak shifting in the diffraction patterns.

For the 5%-Zr-ss sample, the FT-EXAFS fitting is compatible with the scattering paths extracted from the *m*-Li_2ZrO_3 crystal structure as reported in the Supporting Information, Figure S18. No Zr-M scattering path is observed for this sample, which unequivocally confirms the XRD results that Zr does not diffuse in the active material but only forms as Li_2ZrO_3. Moreover, to get a clear detection of the coordination environment in Zr−Zr and Zr−M, wavelet transform (WT) of Zr *K*-edge EXAFS oscillations according to high resolution in *K* and *R* spaces is carried out. The resulting WT contour plots of the Zr−Zr and Zr−M bonds are shown in Figure 6d,e, respectively. It further confirms that Zr−M is centered at 2.43 $Å^{-1}$ and Zr−Zr is centered at 2.81 $Å^{-1}$.

3.4. Electrochemistry. To correlate the dopant inclusion with cathode performance and stability of the doped/undoped samples, rate capability measurements were carried out for undoped and 0.1 mol % doping for both co-precipitation and lithiation-modified materials. As shown in Figure 7a, the discharging capacity of 0.1%-Zr-cp performs better at 5 C when the cathode material is pushed to a faster lithiation rate during discharge, while at lower C-rates, there is no noticeable/consistent difference. Additionally, 0.1%-Zr-cp shows slightly higher capacity retention after the recovering cycle at 0.2 C compared to the 0.1%-Zr-ss and undoped samples. In fact, after 22 cycles at different C rates, the capacity retention of the 0.1%-Zr-cp, 0.1%-Zr-ss, and undoped samples are 97.7, 96.2, and 96.6% respectively. Furthermore, the samples were also galvanostatically investigated for 100 cycles at 1 C. As shown in Figure 7b, these three samples do not noticeably differ in capacity for the first ∼20 cycles. However, a discrepancy starts to appear after this threshold. After 100 cycles, 0.1%-Zr-cp has a higher capacity retention compared to both the 0.1%-Zr-ss and undoped samples, although 0.1%-Zr-ss seems to have initially a slightly higher capacity over the undoped sample. The excellent capacity retention of the modified material is comparable to other composite Ni-rich electrodes at 1 C.[46] It is important to underline that the specific capacity recorded at 1 C for the rate capability tests does not show the same discrepancy as that per the long-term cycling test. This is not unexpected, since the two measurement modes are not directly comparable. The long-term cycling program is different for the charging process as explained in Section 2.2. Moreover, Supporting Information Figure S26 reports the difference in cycling program between rate capability and long-term cycling.

Furthermore, the dQ/dV analysis vs voltage plots calculated for the long-term cycling tests as presented in Supporting Figures S23−S25 show no distinct differences at the fourth cycle when the electrodes can still be considered fresh indicating that these three samples behave similarly. However, at the 50th cycle during the charging process at the $H2 \rightarrow H3$ transition (ca. 4.25 V), 0.1%-Zr-cp, shows a shift to lower values in the redox potentials compared to those of the 0.1%-Zr-ss and undoped sample. The slight shift to lower voltages for the 0.1 mol % sample modified upon co-precipitation is attributed to lower overpotentials needed for the lithium extraction from the host structure. Furthermore, the $H2 \rightarrow H3$ discharge process takes place at higher voltages for 0.1%-Zr-cp, which shortens the ΔV, defining not only faster kinetics during the charging process but also improved reversibility for Li^+ deintercalation/intercalation.

Given that the 0.1%-Zr-ss sample exhibits slightly poorer performance upon cycling, additional electrochemical studies were conducted in full cells to increase the number of cycles. The utilization of graphite and additives in carbonated-based electrolytes is necessary to mitigate anodic instability in half-cells.[47] Results from long-term cycling in full cells, as depicted in Figure S27, reveal that 0.1%-Zr-ss suffers from notable capacity loss after 850 cycles. Moreover, 0.1%-Zr-cp continues to demonstrate a slightly superior capacity retention compared to the undoped sample. Despite the minimal amount of dopant utilized during the co-precipitation step, we expected a small impact on electrochemical performance relative to the undoped sample.

4. CONCLUSIONS

The effect of small traces of Zr doping in MMC811 has been studied through Zr addition in two different co-precipitation synthesis steps: upon lithiation and co-precipitation. Upon the lithiation step, as shown from 0.1%-Zr-ss and a 50 times higher Zr content of 5%-Zr-ss, multiple phase impurities are detected by the means of HR-XRD, and these are ascribed to Li_2ZrO_3 (LZO) polymorphs. The XANES spectra confirmed the same local environment for 5%-Zr-ss and 0.1%-Zr-ss. Therefore, it is concluded that through this step bulk doping is unlikely to happen since Zr^{4+} finds a more thermodynamically stable structure compared to incorporation in the active material.

https://doi.org/10.1021/acsami.4c05058
ACS Appl. Mater. Interfaces XXXX, XXX, XXX−XXX

Furthermore, SEM-EDX suggests that no coating on top of the NMC811 particles occurs.

Zr doping through the co-precipitation method shows no extra phases. Zr is bulk doped and octahedrally coordinated in the NMC811 phase with bond lengths compatible with those of the TM site. Zr doping in this case provides more structural stability and enhancement of capacity retention. The dopant behavior in the two different steps remains true for trace amounts where no multiple mechanisms are observed. The employment of synchrotron radiation allowed us to detect weak features otherwise hidden by the usual laboratory techniques. Understanding the doping process and the role of the dopant in material performance and stabilization is an important step to effectively engineer the doped NMC811 materials.

■ ASSOCIATED CONTENT

Supporting Information

The Supporting Information is available free of charge at https://pubs.acs.org/doi/10.1021/acsami.4c05058.

Synthesis sketch, materials, and weights used upon calcination; diffraction, multiple-phase analysis, and Rietveld refinement for cation mixing estimation; SEM-EDX of 5% doped NMC811 and TEM-EDX lamella analysis for undoped, 0.1%-Zr-ss, and 0.1%-Zr-cp samples; X-ray spectroscopy (XANES, EXAFS), tetrahedral and octahedral sites fitting, reference Zr foil fit, Ni, Co, and Mn additional XANES spectra; dq/dV analysis of long-term cycling data; and ICP-OES and XRF analysis for elemental quantification (PDF)

■ AUTHOR INFORMATION

Corresponding Authors

Tobias Schulli − *European Synchrotron Radiation Facility, 38000 Grenoble, France*; Email: schulli@esrf.fr

Jakub Drnec − *European Synchrotron Radiation Facility, 38000 Grenoble, France*; Email: drnec@esrf.fr

Tanja Kallio − *Department of Chemistry and Material Science, School of Chemical Engineering, Aalto University, 02150 Espoo, Finland*; orcid.org/0000-0001-6671-8582; Email: tanja.kallio@aalto.fi

Authors

Mattia Colalongo − *European Synchrotron Radiation Facility, 38000 Grenoble, France; Department of Chemistry and Material Science, School of Chemical Engineering, Aalto University, 02150 Espoo, Finland*; orcid.org/0000-0003-3511-641X

Basit Ali − *Department of Chemistry and Material Science, School of Chemical Engineering, Aalto University, 02150 Espoo, Finland*; orcid.org/0000-0002-6272-486X

Isaac Martens − *European Synchrotron Radiation Facility, 38000 Grenoble, France*

Marta Mirolo − *European Synchrotron Radiation Facility, 38000 Grenoble, France*; orcid.org/0000-0002-6781-2762

Ekaterina Laakso − *Department of Chemistry and Material Science, School of Chemical Engineering, Aalto University, 02150 Espoo, Finland; Department of Engineering Science, Separation Science, School of LUT University, 53850 Lappeenranta, Finland*

Cesare Atzori − *European Synchrotron Radiation Facility, 38000 Grenoble, France*; orcid.org/0000-0002-3227-7421

Giorgia Confalonieri − *European Synchrotron Radiation Facility, 38000 Grenoble, France*; orcid.org/0000-0002-4535-9354

Peter Kus − *Department of Surface and Plasma Science, Faculty of Mathematics and Physics, Charles University, 18000 Prague 8, Czech Republic*; orcid.org/0000-0002-2246-4426

Anna Kobets − *Department of Chemistry and Material Science, School of Chemical Engineering, Aalto University, 02150 Espoo, Finland*

Xiangze Kong − *Department of Chemistry and Material Science, School of Chemical Engineering, Aalto University, 02150 Espoo, Finland*

Timo Kankaanpää − *Umicore Battery Materials Finland Oy, 67101 Kokkola, Finland*

Complete contact information is available at: https://pubs.acs.org/10.1021/acsami.4c05058

Author Contributions

M.C. designed and performed the experiments, analyzed the data, and wrote the paper. T.K., T.K., T.S., J.D., and B.A. supervised the project. M.M., I.M., C.A., T.S., T.K., T.K, G.C., J.D., and B.A. actively participated in the scientific discussion, and review editing. C.A. local contacted and supervised the XAS experiment at BM23, B.A. contributed to the XAS data interpretation and cosupervised the project. I.M. supervised the HE-XRD experiment at ID31, G.C. performed the HR-XRD measurements at ID22. T.K. provided the precursor materials and performed the ICP-XRF measurements. E.L. synthesized the materials for the XAS experiment. P.K. performed the SEM-EDX measurements and contributed to the interpretation of the data. B.A. performed FIB cutting and TEM measurements. K.X. and A.K. performed full-cells electrochemical tests.

Notes

The authors declare no competing financial interest.

■ ACKNOWLEDGMENTS

This project has received funding from the European Union's Horizon 2020 research and innovation programme under the Marie Skłodowska-Curie grant agreement No 847439. We acknowledge the European Synchrotron Radiation Facility(ESFR) for provision of synchrotron radiation facilities at the ID31 beamline (IHCH1603), BM23 (BLC1559), ID22 (IHCH3772), Aalto University for utilizing the RAw Materials Infrastructure (RAMI) and Campus France (grant PHC Barrande 46755RA) for mobility funding.

■ REFERENCES

(1) Andre, D.; Kim, S.-J.; Lamp, P.; Lux, S. F.; Maglia, F.; Paschos, O.; Stiaszny, B. Future Generations of Cathode Materials: an Automotive Industry Perspective. *Journal of Materials Chemistry A* **2015**, *3*, 6709−6732.

(2) Myung, S.-T.; Maglia, F.; Park, K.-J.; Seung Yoon, C.; Lamp, P.; Kim, S.-J.; Sun, Y.-K Nickel-Rich Layered Cathode Materials for Automotive Lithium-Ion Batteries: Achievements and Perspectives. *ACS Energy Lett.* **2017**, *2*, 196−223.

(3) Yoon, C. S.; Jun, D.-W.; Myung, S.-T.; Sun, Y.-K. Structural Stability of LiNiO2 Cycled above 4.2 V. *ACS Energy Lett.* **2017**, *2*, 1150−1155.

(4) Kalyani, P.; Kalaiselvi, N. Various Aspects of LiNiO2 Chemistry: A Review. *Sci. Technol. Adv. Mater.* **2005**, *6*, 689−703.
(5) Wang, Q.; Shen, C.-H.; Shen, S.-Y.; Xu, Y.-F.; Shi, C.-G.; Huang, L.; Li, J.-T.; Sun, S.-G. Origin of Structural Evolution in Capacity Degradation for Overcharged NMC622 via Operando Coupled Investigation. *ACS Appl. Mater. Interfaces* **2017**, *9*, 24731−24742.
(6) Chen, J.; Yang, H.; Li, T.; Liu, C.; Tong, H.; Chen, J.; Liu, Z.; Xia, L.; Chen, Z.; Duan, J.; Li, L. The Effects of Reversibility of H2-H3 Phase Transition on Ni-Rich Layered Oxide Cathode for High-Energy Lithium-Ion Batteries. *Front. Chem.* **2019**, *7*, 500.
(7) Cheng, X.; Zheng, J.; Lu, J.; Li, Y.; Yan, P.; Zhang, Y. Realizing Superior Cycling Stability of Ni-Rich Layered Cathode by Combination of Grain Boundary Engineering and Surface Coating. *Nano Energy* **2019**, *62*, 30−37.
(8) Yan, P.; Zheng, J.; Liu, J.; Wang, B.; Cheng, X.; Zhang, Y.; Sun, X.; Wang, C.; Zhang, J.-G. Tailoring Grain Boundary Structures and Chemistry of Ni-Rich Layered Cathodes for Enhanced Cycle Stability of Lithium-Ion Batteries. *Nature Energy* **2018**, *3*, 600−605.
(9) Zou, L.; Zhao, W.; Liu, Z.; Jia, H.; Zheng, J.; Wang, G.; Yang, Y.; Zhang, J.-G.; Wang, C. Revealing Cycling Rate-Dependent Structure Evolution in Ni-Rich Layered Cathode Materials. *ACS Energy Lett.* **2018**, *3*, 2433−2440.
(10) Dose, W. M.; Temprano, I.; Allen, J. P.; Bjorklund, E.; O'Keefe, C. A.; Li, W.; Mehdi, B. L.; Weatherup, R. S.; De Volder, M. F.; Grey, C. P. Electrolyte Reactivity at The Charged Ni-Rich Cathode Interface and Degradation in Li-Ion Batteries. *ACS Appl. Mater. Interfaces* **2022**, *14*, 13206−13222.
(11) Li, J.; Liang, G.; Zheng, W.; Zhang, S.; Davey, K.; Pang, W. K.; Guo, Z. Addressing cation mixing in layered structured cathodes for lithium-ion batteries: A critical review. *Nano Materials Science* **2023**, *5*, 404−420.
(12) Yan, P.; Zheng, J.; Lv, D.; Wei, Y.; Zheng, J.; Wang, Z.; Kuppan, S.; Yu, J.; Luo, L.; Edwards, D.; Olszta, M.; Amine, K.; Liu, J.; Xiao, J.; Pan, F.; Chen, G.; Zhang, J.-G.; Wang, C.-M. Atomic-Resolution Visualization of Distinctive Chemical Mixing Behavior of Ni, Co, and Mn with Li in Layered Lithium Transition-Metal Oxide Cathode Materials. *Chem. Mater.* **2015**, *27*, 5393−5401.
(13) Liu, S.; Dang, Z.; Liu, D.; Zhang, C.; Huang, T.; Yu, A. Comparative Studies of Zirconium Doping and Coating on LiNi0.6Co0.2Mn0.2O2 Cathode Material at Elevated Temperatures. *J. Power Sources* **2018**, *396*, 288−296.
(14) Schipper, F.; Bouzaglo, H.; Dixit, M.; Erickson, E. M.; Weigel, T.; Talianker, M.; Grinblat, J.; Burstein, L.; Schmidt, M.; Lampert, J.; Erk, C.; Markovsky, B.; Major, D. T.; Aurbach, D. From Surface ZrO2 Coating to Bulk Zr Doping by High Temperature Annealing of Nickel-Rich Lithiated Oxides and Their Enhanced Electrochemical Performance in Lithium Ion Batteries. *Adv. Energy Mater.* **2018**, *8*, No. 1701682.
(15) Schipper, F.; Dixit, M.; Kovacheva, D.; Talianker, M.; Haik, O.; Grinblat, J.; Erickson, E. M.; Ghanty, C.; Major, D. T.; Markovsky, B.; Aurbach, D. Stabilizing Nickel-Rich Layered Cathode Materials by a High-Charge Cation Doping Strategy: Zirconium-Doped LiNi0.6-Co0.2Mn0.2O2. *Journal of Materials Chemistry A* **2016**, *4*, 16073−16084.
(16) Sharma, A.; Rajkamal, A.; Kobi, S.; Kumar, B. S.; Paidi, A. K.; Chatterjee, A.; Mukhopadhyay, A. Addressing the High-Voltage Structural and Electrochemical Instability of Ni-Containing Layered Transition Metal (T M) Oxide Cathodes by "Blocking" the "T M -Migration" Pathway in the Lattice. *ACS Appl. Mater. Interfaces* **2021**, *13*, 25836−25849.
(17) Park, K.; Ham, D. J.; Park, S. Y.; Jang, J.; Yeon, D.-H.; Moon, S.; Ahn, S. J. High-Ni cathode material improved with Zr for stable cycling of Li-ion rechargeable batteries. *RSC Adv.* **2020**, *10*, 26756−26764.
(18) Ou, X.; Liu, T.; Zhong, W.; Fan, X.; Guo, X.; Huang, X.; Cao, L.; Hu, J.; Zhang, B.; Chu, Y. S.; Hu, G.; Lin, Z.; Dahbi, M.; Alami, J.; Amine, K.; Yang, C.; Lu, J. Enabling high energy lithium metal batteries via single-crystal Ni-rich cathode material co-doping strategy. *Nat. Commun.* **2022**, *13*, 2319.
(19) Choi, J.; Lee, S.-Y.; Yoon, S.; Kim, K.-H.; Kim, M.; Hong, S.-H. The Role of Zr Doping in Stabilizing Li[Ni0.6Co0.2Mn0.2]O2 as a Cathode Material for Lithium-Ion Batteries. *ChemSusChem* **2019**, *12*, 2439−2446.
(20) Sivaprakash, S.; Majumder, S. Understanding the role of Zr4+ cation in improving the cycleability of LiNi0. 8Co0. 15Zr0. 05O2 cathodes for Li ion rechargeable batteries. *Journal of alloys and compounds* **2009**, *479*, 561−568.
(21) Fitch, A.; Dejoie, C.; Covacci, E.; Confalonieri, G.; Grendal, O.; Claustre, L.; Guillou, P.; Kieffer, J.; de Nolf, W.; Petitdemange, S.; Ruat, M.; Watier, Y. ID22 − the high-resolution powder-diffraction beamline at ESRF. *Journal of Synchrotron Radiation* **2023**, *30*, 1003−1012.
(22) Toby, B. H.; Von Dreele, R. B. *GSAS-II*: The Genesis of a Modern Open-Source All Purpose Crystallography Software Package. *J. Appl. Crystallogr.* **2013**, *46*, 544−549.
(23) Mathon, O.; Beteva, A.; Borrel, J.; Bugnazet, D.; Gatla, S.; Hino, R.; Kantor, I.; Mairs, T.; Munoz, M.; Pasternak, S.; Perrin, F.; Pascarelli, S. The Time-Resolved and Extreme Conditions XAS (TEXAS) Facility at The European Synchrotron Radiation Facility: the General-Purpose EXAFS Bending-Magnet Beamline BM23. *Journal of synchrotron radiation* **2015**, *22*, 1548−1554.
(24) Ravel, B.; Newville, M. *ATHENA, ARTEMIS, HEPHAESTUS*: Data Analysis For X-Ray Absorption Spectroscopy Uing *IFEFFIT*. *Journal of Synchrotron Radiation* **2005**, *12*, 537−541.
(25) Gao, S.; Zhan, X.; Cheng, Y.-T. Structural, Electrochemical and Li-Ion Transport Properties of Zr-Modified LiNi0.8Co0.1Mn0.1O2 Positive Electrode Materials for Li-Ion Batteries. *J. Power Sources* **2019**, *410−411*, 45−52.
(26) Li, X.; Zhang, K.; Wang, M.; Liu, Y.; Qu, M.; Zhao, W.; Zheng, J. Dual Functions of Zirconium Modification on Improving the Electrochemical Performance of Ni-rich LiNi0.8Co0.1Mn0.1O2. *Sustainable. Energy Fuels* **2018**, *2*, 413−421.
(27) Gao, Y.; Park, J.; Liang, X. Comprehensive Study of Al- And Zr-Modified LiNi0.8Mn0.1Co0.1O2 through Synergy of Coating and Doping. *ACS Applied Energy Materials* **2020**, *3*, 8978−8987.
(28) Quintana, P.; Leal, J.; Howie, R. A.; West, A. R. Li2ZrO3: A new polymorph with the $alpha$-LiFeO2 Structure. *Mater. Res. Bull.* **1989**, *24*, 1385−1389.
(29) Orsetti, N. G.; Gamba, M.; Gómez, S.; Yasnó, J. P.; Suárez, G. The Transcendental Role of Lithium Zirconates in the Development of Modern Energy Technologies. *Ceram. Int.* **2022**, *48*, 8930−8959.
(30) Yasnó, J. P.; Conconi, S.; Visintin, A.; Suárez, G. Non-Isothermal Reaction Mechanism and Kinetic Analysis for the Synthesis of Monoclinic Lithium Zirconate (m-Li2ZrO3) during Solid-State Reaction. *J. Anal. Sci. Technol.* **2021**, *12*, 15.
(31) Fujii, Y.; Miura, H.; Suzuki, N.; Shoji, T.; Nakayama, N. Structural and Electrochemical Properties of LiNi1/3Co1/3Mn1/3O2: Calcination Temperature Dependence. *J. Power Sources* **2007**, *171*, 894−903.
(32) Wu, H.; Zhou, X.; Yang, C.; Xu, D.; Zhu, Y.-H.; Zhou, T.; Xin, S.; You, Y. Concentration-gradient Nb-doping in a single-crystal LiNi0. 83Co0. 12Mn0. 05O2 cathode for high-rate and long-cycle lithium-ion batteries. *ACS Appl. Mater. Interfaces* **2023**, *15*, 18828−18835.
(33) Williamson, G.; Hall, W. X-ray Line Broadening from Filed Aluminium and Wolfram. *Acta Metall.* **1953**, *1*, 22−31.
(34) Orlova, E. D.; Savina, A. A.; Abakumov, S. A.; Morozov, A. V.; Abakumov, A. M. Comprehensive Study of Li+/Ni2+ Disorder in Ni-Rich NMCs Cathodes for Li-Ion Batteries. *Symmetry* **2021**, *13*, 1628.
(35) Zhu, J.; Vo, T.; Li, D.; Lu, R.; Kinsinger, N. M.; Xiong, L.; Yan, Y.; Kisailus, D. Crystal growth of Li [Ni1/3Co1/3Mn1/3] O2 as a cathode material for high-performance lithium ion batteries. *Cryst. Growth Des.* **2012**, *12*, 1118−1123.
(36) Wang, T.; Ren, K.; He, M.; Dong, W.; Xiao, W.; Pan, H.; Yang, J.; Yang, Y.; Liu, P.; Cao, Z.; Ma, X.; Wang, H. Synthesis and Manipulation of Single-Crystalline Lithium Nickel Manganese Cobalt Oxide Cathodes: A Review of Growth Mechanism. *Front. Chem.* **2020**, *8*, 747.

https://doi.org/10.1021/acsami.4c05058
ACS Appl. Mater. Interfaces XXXX, XXX, XXX−XXX

(37) Greegor, R.; Blohowiak, K.; Osborne, J.; Krienke, K.; Cherian, J.; Lytle, F. X-ray Spectroscopic Investigation of the Zr-Site in Thin Film Sol-Gel Surface Preparations. *J. Sol-Gel Sci. Technol.* **2001**, *20*, 35−50.
(38) Sanchez, C.; In, M. Molecular Design of Alkoxide Precursors for the Synthesis of Hybrid Organic-Inorganic Gels. *Journal of non-crystalline solids* **1992**, *147*, 1−12.
(39) Finkeldei, S.; Stennett, M.; Kowalski, P.; Ji, Y.; de Visser-Tỳnová, E.; Hyatt, N.; Bosbach, D.; Brandt, F. Insights into the Fabrication and Structure of Plutonium Pyrochlores. *Journal of Materials Chemistry A* **2020**, *8*, 2387−2403.
(40) Ghosh, P.; Priolkar, K. R.; Patra, A. Understanding the Local Structures of Eu and Zr in Eu2O3 Doped and Coated ZrO2 Nanocrystals by EXAFS Study. *J. Phys. Chem. C* **2007**, *111*, 571−578.
(41) Nakai, I.; Shibai, Y.; Murakami, Y. XANES Study in the Solid State Reaction of Zr−Ni System. *Journal of Synchrotron Radiation* **2001**, *8*, 815−817.
(42) Prestipino, C.; Mathon, O.; Hino, R.; Beteva, A.; Pascarelli, S. Quick-EXAFS implementation on the general purpose EXAFS beamline at ESRF. *Journal of synchrotron radiation* **2011**, *18*, 176−182.
(43) Erickson, E. M.; Sclar, H.; Schipper, F.; Liu, J.; Tian, R.; Ghanty, C.; Burstein, L.; Leifer, N.; Grinblat, J.; Talianker, M.; Shin, J.; Lampert, J. K.; Markovsky, B.; Frenkel, A. I.; Aurbach, D. High-Temperature Treatment of Li-Rich Cathode Materials with Ammonia: Improved Capacity and Mean Voltage Stability during Cycling. *Adv. Energy Mater.* **2017**, *7*, No. 1700708.
(44) Ahrens, L. H. The use of ionization potentials Part 1. Ionic Radii of the Elements. *Geochim. Cosmochim. Acta* **1952**, *2*, 155−169.
(45) Lu, Y.; Pang, M.; Shi, S.; Ye, Q.; Tian, Z.; Wang, T. Enhanced Electrochemical Properties of Zr4+-Doped Li1.20 [Mn0.52Ni0.20Co0.08]O2 Cathode Material for Lithium-Ion Battery at Elevated Temperature. *Sci. Rep.* **2018**, *8*, 2981.
(46) Liu, C.; Miao, C.; He, M.; Wang, J.; Chen, Q.; Nie, S.; Xiao, W. Optimized layered ternary LiNi0.5Co0.2Mn0.3O2 cathode materials modified with ultrathin Li3InCl6 fast ion conductor layer for lithium-ion batteries. *J. Power Sources* **2023**, *566*, No. 232961.
(47) Fan, X.; Chen, L.; Borodin, O.; Ji, X.; Chen, J.; Hou, S.; Deng, T.; Zheng, J.; Yang, C.; Liou, S.-C.; et al. Non-flammable electrolyte enables Li-metal batteries with aggressive cathode chemistries. *Nature Nanotechnol.* **2018**, *13*, 715−722.

https://doi.org/10.1021/acsami.4c05058
ACS Appl. Mater. Interfaces XXXX, XXX, XXX−XXX